Local plastic deformation in the vicinity of topologically close-packed phases in a Ni-based single crystal superalloy

Sangwon Lee [a,b,c], Jeonghyeon Do [b], Baig Gyu Choi [b], Ujjval Bansal [c], Christoph Kirchlechner [c], Pyuck-Pa Choi [a,*], Subin Lee [c,*]

[a] Department of Materials Science and Engineering, Korea Advanced Institute of Science and Technology (KAIST), Daejeon 34141 Republic of Korea
[b] Department of High Temperature Materials, Korea Institute of Materials Science (KIMS), Changwon 51508 Republic of Korea
[c] Institute for Applied Materials, Karlsruhe Institute of Technology, Karlsruhe 76131 Germany

ARTICLE INFO

ABSTRACT

The role of a topologically close-packed (TCP) phase (μ phase) on the plastic deformation of a Ni-based super-alloy was investigated employing a combination of *in situ* scanning electron microscope micropillar compression and atomic-scale characterization using atom probe tomography and transmission electron microscopy. Micro-pillar tests revealed two distinct slip behaviors: TCP-free pillars deformed via multiple slip systems, whereas TCP-containing pillars deformed by single slip. Notably, while previous studies have reported fracture at the TCP/γ' interface, our findings revealed that in the TCP-containing pillars, deformation was rarely observed at the interface. Instead, slip predominantly occurred in regions approximately 50–100 nm away from the interface. Chemical analysis near the TCP/γ' interface via APT showed an excess Ta content near the interface increasing the antiphase boundary energy and enhancing local order strengthening. Moreover, an approximate 8% lattice misfit at the TCP/γ' interface, coupled with the elastic mismatch between the two phases, provided additional slip resistance in the vicinity of the interface. This study sheds light on the intricate interplay between TCP phase formation, microstructural evolution, and mechanical properties in Ni-based superalloys offering valuable insights into the role of the TCP phases.

1. Introduction

In the aerospace and power generation industries, single-crystalline nickel (Ni)-based superalloys have been widely used in turbine blades owing to their outstanding creep and fatigue properties [1]. With the aim of improved energy efficiency in gas turbines and reduction in CO_2 emissions, there arises an increasing demand for their higher operating temperatures [1–5]. Accordingly, the design of modern Ni-based superalloys has prioritized the enhancement of the high-temperature properties, particularly creep life and strength, which can be achieved through the addition of refractory elements with high melting points and low diffusivities, such as Re, Mo, Cr, and W [6–10]. However, due to their sluggish diffusion, these refractory elements remain partitioned to the dendrite core even after a solution heat-treatment process [11–13], promoting the precipitation of topologically close-packed (TCP) phases during long-term service under high-temperature environments [1,13–16].

The formation of TCP phases has been recognized as a detrimental factor that degrades microstructural stability and mechanical properties, consequently shortening service life [17–20]. TCP phases are known to act as crack initiation sites under creep and fatigue loading [21–24], through two proposed mechanisms. Firstly, they induce a depletion and subsequent softening of the γ matrix. As TCP phases consume a significant amount of refractory elements from the surrounding γ matrix, e.g. W, Re, Cr, and Mo, they trigger the dissolution of the γ matrix during the nucleation and growth of TCP phases [25]. This undesirable microstructural evolution not only leads to the collapse of the cuboidal γ/γ' structure but also to the softening of the γ matrix due to the depletion of solid solution strengthening elements [21,22]. Secondly, fractures of the TCP phases may occur. TCP phases themselves exhibit brittleness due to their directional bonding [1]. Also, the TCP/γ' interface shows weak coherency and bond strength [23]. Thus, crystalline defects, such as dislocations or stacking faults, are accumulated at the TCP/γ' interface and finally cracking occurs inside the TCP phases or at the TCP/γ' interface during deformation [23,24,26,27].

Despite the significant importance of mechanical degradation

Table 1
Nominal composition of the single-crystal Ni-based superalloy (wt.%).

Ni	Al + Ti + Ta	Co + Cr + Mo + W
Bal.	14.8	27.6

induced by TCP phases on material reliability under extreme environments, the deformation behavior associated with the TCP phases remains not fully understood. Previous studies have primarily relied on post-mortem analysis of crack distributions after macro-scale mechanical testing [21–27], and the direct correlation of mechanical properties with TCP phase distributions has been rarely reported mainly due to the nanometer-scale precipitate sizes. Complicating matters further, TCP-related deformation behavior is profoundly influenced by the types of phases (e.g., μ, σ, P, and R) and their morphologies (e.g., plate-like, needle-like, and spherical). Regarding the cracking behavior of the TCP phases, contradictory observations have been reported. For example, while Chen et al. [28] and Pessah et al. [21] reported internal cracks in plate-like σ and μ phases, others have not observed cracks in needle-like and plate-like μ phases following macroscopic creep tests [29,30].

To overcome these limitations in investigating sub-micron scale γ, γ', and TCP phases, in-situ micropillar compression testing has emerged as a useful tool for understanding local mechanical behavior. This approach has been employed in various Ni-based superalloy studies [31–34]. For instance, Haußmann et al. [31] conducted comparative studies between dendrite and interdendrite regions to evaluate local property variations, while Kalchev et al. [32] measured the strength and Young's modulus of superalloy thin films. Bhowmik et al. [33] utilized this technique for in-situ observation of γ/γ' rotation behavior, and Arora et al. [34] investigated the influence of lattice misfit on micropillar size effects.

Despite these advances in small-scale mechanical testing of superalloys, the local deformation behavior of the γ/γ' microstructures containing TCP phases remains unexplored. While a recent study by Luo et al. [35] demonstrated the activation of slip systems and determining the critical resolved shear stress (CRSS) in isolated μ-CoNb6 phase via micropillar tests, comprehensive understanding of deformation behavior in the TCP-containing superalloys is still lacking. Thus, further research is required to explore the local deformation behavior in microstructures composed of γ, γ', and TCP phase.

This study aims to elucidate the role of TCP phases on the mechanical properties and deformation behavior of a Ni-based superalloy via micromechanical testing and atomic-scale chemical analysis. To evaluate the differences in slip behavior arising from TCP phases, we conducted *in situ* scanning electron microscope (SEM) micropillar compression tests for statistical analysis and direct observation of crystal defects. Subsequently, a detailed microstructure analysis after deformation was carried out using transmission electron microscopy (TEM), focusing specifically on the plastic deformation near the TCP/γ' interface. The latter is expected to be the initiation site for cracks or plastic deformation. Lastly, atom probe tomography (APT) was employed to investigate compositional factors influencing deformation behavior.

2. Experimental procedures

The composition of the single-crystal Ni-based superalloy used in this study is listed in Table 1. A bulk single-crystal alloy was cast via directional solidification using the Bridgman vacuum induction melting method. The cast material was solutionized at 1300°C for 1 h under an Ar atmosphere, followed by a two-step aging treatment at 1140°C for 2 h and 871°C for 20 h to obtain a γ/γ' microstructure, which is referred as "unexposed". Subsequently, a part of the aged specimen was exposed at 1000°C for 30 min to induce TCP phase precipitation, which is referred as "exposed".

For the microstructure analysis, specimens were firstly mechanically ground with SiC paper from #80 to #2000, and sequentially polished with monocrystalline diamond suspensions (3 and 1 μm) and a colloidal silica suspension (0.25 μm). The polished surface was etched in a solution of 3 g of $CuCl_2$, 30 ml of HCl, and 70 ml of ethanol. The microstructure was observed using a field emission SEM (FE-SEM, SU-5000, Hitachi) equipped with a backscattered electron (BSE) detector.

To evaluate the mechanical properties at the micrometer scale, micropillars with a diameter of 1 μm and a height of 2 μm were fabricated by using a focused ion beam workstation (FIB, Crossbeam 550L, Zeiss). For the unexposed sample, 6 pillars were prepared from TCP-free regions, while for the exposed sample, 19 pillars were prepared from TCP-containing regions to test various conditions, including different
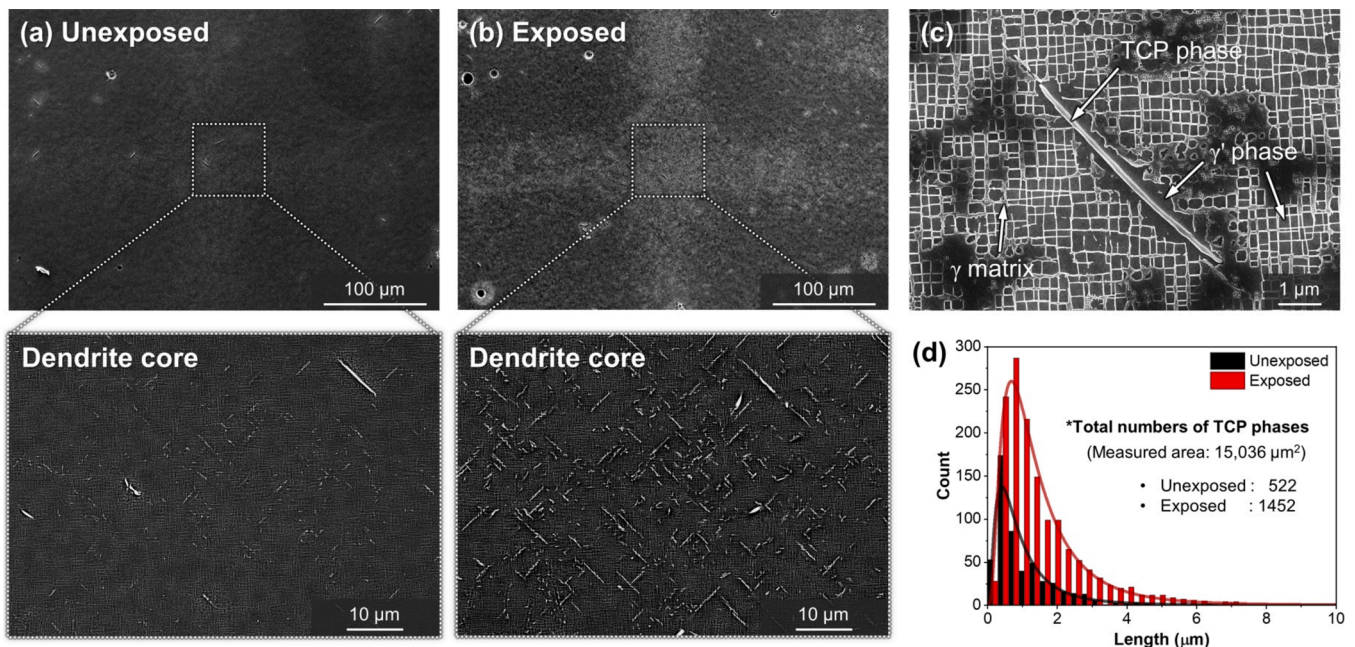
Fig. 1. BSE images observed at [001] orientation of single crystal alloy **(a)** before and **(b)** after high-temperature exposure, showing the distribution of TCP phase in dendrite core. **(c)** A magnified image of γ/γ'/TCP microstructure in the exposed specimen, and **(d)** a size distribution of TCP phases in each state.
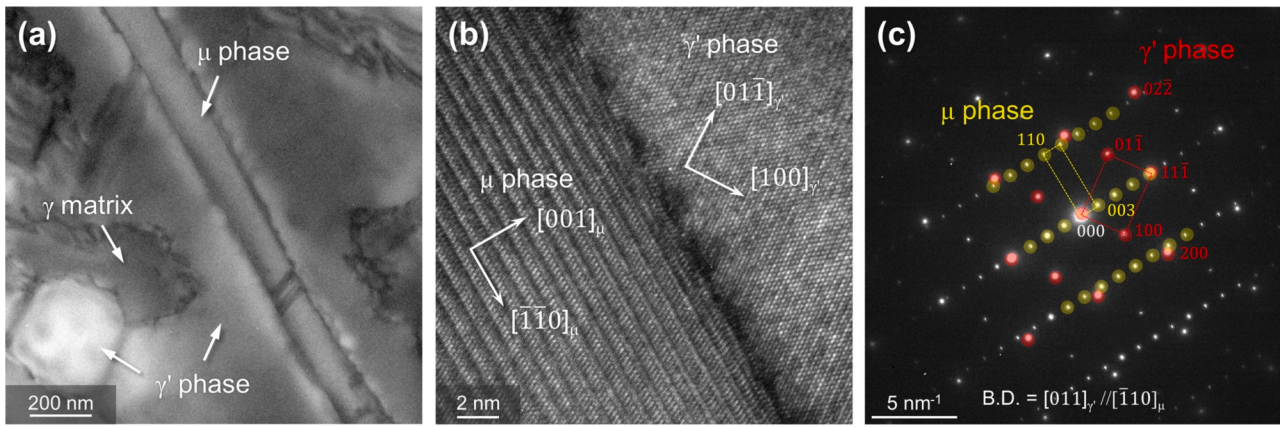
Fig. 2. (a) TEM bright field image showing the γ, γ', and TCP phase region. **(b)** HR TEM image revealing a flat interface between TCP and γ' phase, and **(c)** a selected area electron diffraction pattern from the TCP/γ' interface showing the orientation relationship between the two phases.

orientations, volume fractions, and sizes of TCP phases. Note that TCP-free pillars from the exposed sample were not prepared due to the high density of TCP phases. For the milling process, Ga^+ ions at 30 keV were utilized, with the current set of 30 nA for rough milling, 3 nA for intermediate milling, and 0.7 nA for final milling. The taper angle was kept below 3°. The crystallographic orientations of the pillars with respect to the loading direction were measured by using an electron backscatter diffraction (EBSD). *In situ* SEM micropillar compression tests were performed in a FE-SEM (Merlin, Zeiss) using an *in situ* indenter (Hysitron PI-89, Bruker) in a displacement-controlled mode with a loading rate of 2 nm/s, which is translated into a strain rate of 10^{-3}. A diamond flat punch indenter with a diameter of 2 μm (Synton MDP) was used.

The microstructure of the as-prepared samples was analyzed using a TEM (Tecnai G2 F30, Thermo Fisher Scientific) operated at 300 kV. TEM samples were prepared by jet-polishing (TenuPol-5, Struers) with a voltage of 15 V, a current of 42 mA, and a temperature of −26°C with a solution of 10 % $HClO_4$ in ethanol. The TCP phase and its orientation relationship with respect to the neighboring phases were identified using electron diffraction pattern analysis and high-resolution (HR) TEM imaging. In the case of the analysis of the deformed micropillars, TEM samples were prepared by FIB lift-out (Crossbeam 550L, Zeiss). The TEM lamella containing the pillar underwent coarse milling at 30 kV-300 pA to attain a thickness of 0.9 to 1 μm. This process was followed by a series of fine milling steps: first, 30 kV-100 pA until reaching 500 nm, then 30 kV-50 pA until 200 nm, and finally, 30 kV-20 pA to achieve a thickness close to 100 nm. Subsequent cleaning of the lamella was conducted at 2 kV-10 pA. High-angle annular dark field (HAADF)-scanning transmission electron micrographs (STEM) were acquired using an aberration-corrected STEM (Themis 300, Thermo Fisher Scientific) operated at 300 kV. Composition maps were obtained using energy dispersive spectroscopy (EDS) using a Super-X detector.

The compositions of the TCP-free and TCP-containing regions were characterized by APT (LEAP 4000X HR, Cameca) at a base temperature of 50 K, a detection rate of 0.5%, a laser energy of 60 pJ, and a pulse frequency of 125 kHz. The APT tips were fabricated by using a FIB (Helios G4, Thermo Fisher Scientific). The APT data were reconstructed and analyzed using AP Suite 6.3 program (Cameca).

3. Results

3.1. Formation of the TCP phase during the high-temperature exposure

Fig. 1(a) shows BSE micrographs of the unexposed sample exhibiting a typical $\langle 110 \rangle_{\gamma/\gamma'}$ dendritic structure represented by slightly bright contrast due to Z-contrast imaging. In the dendrite core, TCP phases of a plate-like shape with bright contrast were observed, attributed to the
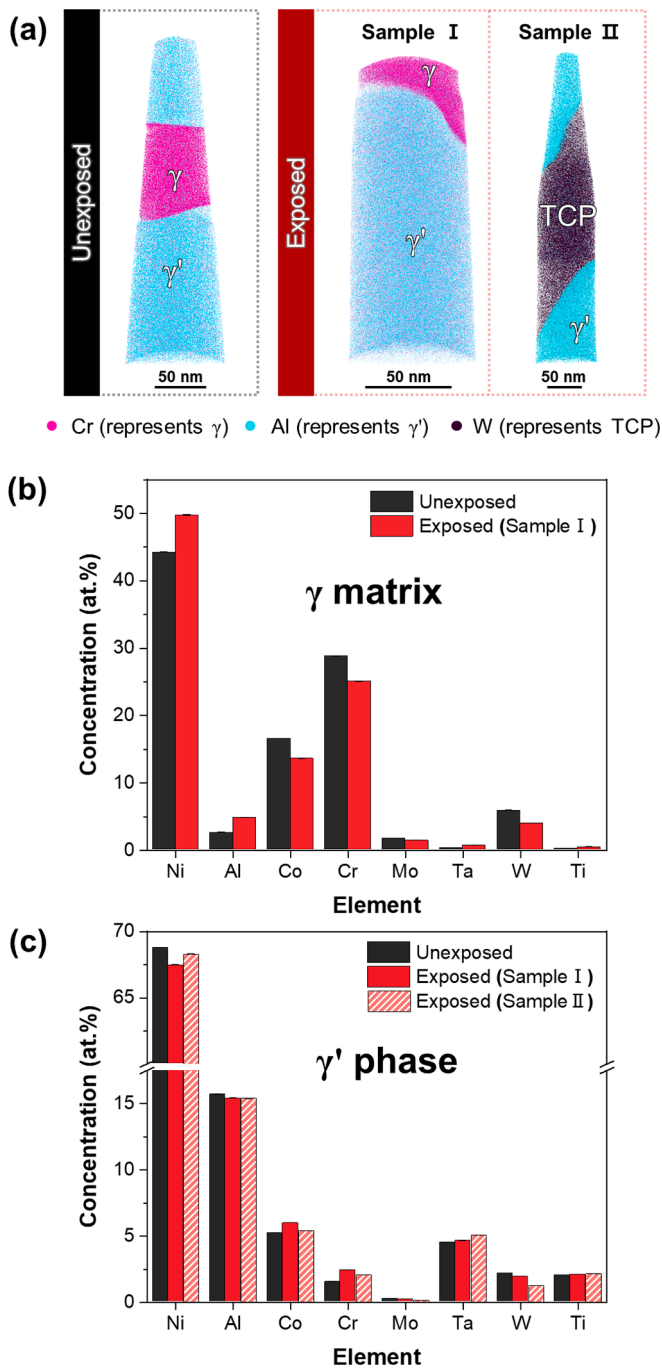
high concentrations of TCP-forming elements such as Cr, Co, and W [23,36]. However, the exposed sample exhibited more easily identifiable dendritic regions due to the high density of TCP phases (Fig. 1(b)). TCP phases were elongated along $\langle 110 \rangle_{\gamma/\gamma'}$ and surrounded by the γ' phase (see Fig. 1(c)). During the growth of the TCP phases, they consumed γ-forming elements resulting in the dissolution of the surrounding γ phase and the formation of γ' envelopes in their vicinity [25].

To quantitatively evaluate TCP phase evolution after the high-temperature exposure, the number density and size of the TCP phases were measured in dendrite core regions (Fig. 1(d)). The number density and length of the TCP phase were increased from 0.03 ± 0.002 to 0.10 ± 0.005 μm^{-2} and from 1.1 ± 0.06 to 1.6 ± 0.04 μm, respectively. Errors denote the standard deviations of the measured values from three images for each specimen.

The crystallography and morphology of an individual TCP phase precipitate were analyzed using TEM imaging and electron diffraction (Fig. 2). Firstly, as observed in SEM-BSE images in Fig. 1, a cross-section of a plate-like TCP phase showed that the TCP phase was surrounded by the γ' phase (Fig. 2(a)). Based on the HR-TEM image (Fig. 2(b)) and electron diffraction patterns (Fig. 2(c)), the crystallographic phase of the TCP phases was identified as the rhombohedral μ phase, which shows a crystal structure belonging to the $R\bar{3}m$ space group [37]. Lattice parameters were determined as $a = 0.48$ nm and $c = 2.59$ nm for the μ phase, while the lattice parameter of γ' was measured as $a = 0.36$ nm. Additionally, the diffraction patterns of the μ and γ' phase indicated the crystallographic orientation relationships between these phases, namely $[011]_{\gamma'}//[\bar{1}10]_{\mu}$, $[\bar{2}1\bar{1}]_{\gamma'}//[110]_{\mu}$, and $[11\bar{1}]_{\gamma'}//[001]_{\mu}$. The planar facet of the plate-like μ phase was determined to be $(001)_{\mu}$ on $\{111\}_{\gamma'}$. The anisotropic morphology of the μ phase and the observed atomic configuration at the interface (Fig. 2(b)) suggested that the TCP/γ' interface is semicoherent and has a small interfacial free energy promoting the growth of precipitates into plate-like shape [38,39]. A further noteworthy finding is the alternating contrast at the interface with regular spacing, suggesting an accumulation of strain at the interface (Fig. 2(b)).

3.2. Compositional changes near the TCP phase

To examine the variations in chemical compositions during high-temperature exposure, APT analyses were conducted on both the unexposed and exposed samples (Fig. 3). The 3D atom maps in Fig. 3(a) illustrate the γ/γ'/TCP phases distinguished by elemental distribution of the Cr-rich γ matrix and the Al-rich γ' phase. Additionally, the W-rich TCP phase and the surrounding γ' phases were detected in another exposed sample, i.e., Sample II. In the γ matrix, the contents of Ni and Al increased by 5.5% and 2.3%, respectively, while Co, Cr, and W

(a)

Unexposed — Exposed — Sample I — Sample II

γ, γ', TCP, γ'

50 nm

• Cr (represents γ)   • Al (represents γ')   • W (represents TCP)

(b) γ matrix

Concentration (at.%) vs Element (Ni, Al, Co, Cr, Mo, Ta, W, Ti)

Legend: Unexposed; Exposed (Sample I)

(c) γ' phase

Concentration (at.%) vs Element (Ni, Al, Co, Cr, Mo, Ta, W, Ti)

Legend: Unexposed; Exposed (Sample I); Exposed (Sample II)

Fig. 3. (a) The 3D atom maps before and after high-temperature exposure process and chemical compositional variations of **(b)** γ matrix and **(c)** γ' phases during the exposure. For the exposed specimen, two samples (at γ/γ' and TCP/γ' regions) were analyzed. The data are listed in Table 2.

decreased by 3.0, 3.7, and 1.9%, respectively, during the exposure process (Fig. 3(b)). These compositional changes can be attributed to the precipitation of the TCP phases. As listed in Table 2, the TCP phase was mainly composed of Co, Cr, and W. Therefore, it could be inferred that the TCP phase consumes the refractory elements from the γ matrix during the nucleation and growth process. On the other hand, for the γ' precipitate, although the compositional changes in Ni, Co, Cr, Ta, and Ta after the exposure process were not as pronounced as in the γ matrix, variations were still observed (Fig. 3(c)). Notably, after the exposure process, there were compositional differences between regions further away from the TCP phase (sample I) and near the TCP phase (sample II).

To investigate the compositional profile near the TCP phase, a proximity histogram of the TCP/γ' interface was obtained from the exposed sample II of Fig. 3(a), which is presented in Fig. 4. This histogram depicts the distribution of alloying elements as a function of the distance from the interface between the TCP phase and the surrounding γ' phase. Refractory elements such as W, Cr, and Mo were found to preferentially partition to the TCP phase, while the γ' precipitate was mainly composed of Ni, Al, and Ta. Furthermore, the histogram revealed segregation of Mo and depletion of Ta on the TCP phase side. On the other hand, on the γ' side, Ta exhibited a peak concentration at the interface, which gradually decreased with the distance from the interface. This compositional profile is attributed to the relatively slow diffusivity of Ta within the γ' phase [40]. As a result, Ta accumulates at the interface rather than in the bulk, since the growth rate of the TCP interface outpaces the diffusion rate of Ta, similar to Re segregation at the γ/γ' interface [41,42]. Consequently, the elemental distribution near the TCP/γ' interface implies that the TCP phase consumes refractory elements while expelling γ'-forming elements to the surrounding γ' phase at high temperature.

3.3. Mechanical behavior at the local region containing the TCP phase

Macroscale mechanical testing and post-mortem analysis of the deformed microstructure have limited utility in understanding the micro-plasticity near the TCP phases because the local strength of microstructure constituents cannot be separated. As described in Section 3.1, the TCP phase precipitates showed a thickness of a few tens of nanometers and were densely distributed with four crystallographic variants. Using FIB-based micromachining, we isolated a few TCP precipitates in the constrained volume of a micropillar, and examined their effects on the deformation behavior and mechanical properties using *in situ* SEM micropillar compression (Fig. 5). Firstly, micropillars of 1 μm in diameter, enclosing the TCP phase, were prepared from the exposed specimens. For comparison, TCP-free pillars of same dimensions were also prepared from the unexposed sample. The loading direction was close to $[001]_{\gamma/\gamma'}$ in both cases. The deviation angles between $[001]_{\gamma/\gamma'}$ and the loading direction were 7.3° and 0.9° for the unexposed and exposed samples, respectively, measured from the EBSD orientation analysis. The TCP phases in the exposed samples were inclined about 55° with respect to the loading direction, i.e., micropillar normal orientation following its orientation relationship with γ/γ'.

Firstly, a clear difference was observed in the slip behavior between two types of micropillars as representative pillars from each type are shown in Fig. 5(a) and (b). In the case of the TCP-free unexposed samples, multiple slip systems were activated as indicated by arrows in the deformed image because 4 out of 12 $\{111\}\langle 1\bar{1}0\rangle_{\gamma/\gamma'}$ slip systems have sufficiently high Schmid factors in the range of 0.43–0.44. Also, the shearing of γ' phase was observed. In the case of TCP-containing exposed samples, on the other hand, only $(\bar{1}11)$ planes parallel to TCP phase (i.e., slip plane 1) were dominantly slipped, and the secondary slip on a slip plane being not parallel to the TCP phase (i.e. slip plane 2) was hindered by the TCP phase (Fig. 5(b)). It is worth noting that although the exposed samples had more favorable orientations for multiple slip activation (i.e., the loading direction is more close to $[001]_{\gamma/\gamma'}$, thus 6 out of 12 $\{111\}\langle 1\bar{1}0\rangle_{\gamma/\gamma'}$ slip systems show similar Schmid factors around 0.41), single slip system has been dominantly activated. This observation implies that the TCP phase limits the activation of other non-parallel slip systems and promotes single slip parallel to the TCP/γ' interface.

The corresponding engineering stress–strain curves are presented in Fig. 6. A total 6 pillars were tested for the unexposed sample with no TCP phases in the pillars, while 19 pillars were tested for the exposed sample containing TCP phases. The SEM images of all deformed pillars are given in Fig. S1 and S2 in the Supplementary material. As observed in the stress–strain curves, the yield strength of the unexposed sample was

Table 2
Chemical compositions of γ, γ', and TCP phase obtained from APT (at.%). For the exposed specimen, two regions (at γ/γ' and TCP/γ' regions) were analyzed.

Phase	Sample	Ni	Al	Co	Cr	Mo	Ta	W	Ti
γ	Unexposed	44.2 (± 0.03)	2.5 (± 0.01)	16.5 (± 0.02)	28.7 (± 0.03)	1.7 (± 0.01)	0.3 (± 0.01)	5.8 (± 0.02)	0.2 (± 0.00)
	Exposed (Sample I)	49.7 (± 0.08)	4.8 (± 0.03)	13.5 (± 0.05)	25.0 (± 0.06)	1.4 (± 0.02)	0.6 (± 0.01)	3.9 (± 0.03)	0.4 (± 0.01)
γ'	Unexposed	68.8 (± 0.02)	15.7 (± 0.01)	5.2 (± 0.01)	1.5 (± 0.00)	0.2 (± 0.00)	4.5 (± 0.01)	2.1 (± 0.00)	2.0 (± 0.00)
	Exposed (Sample I)	67.5 (± 0.02)	15.4 (± 0.01)	5.9 (± 0.01)	2.4 (± 0.01)	0.2 (± 0.00)	4.6 (± 0.01)	1.9 (± 0.01)	2.0 (± 0.00)
	Exposed (Sample II)	68.3 (± 0.02)	15.4 (± 0.01)	5.4 (± 0.01)	2.1 (± 0.01)	0.2 (± 0.00)	5.1 (± 0.01)	1.3 (± 0.01)	2.2 (± 0.01)
TCP	Exposed (Sample II)	21.4 (± 0.19)	0.5 (± 0.00)	15.6 (± 0.01)	22.4 (± 0.01)	4.9 (± 0.20)	2.3 (± 0.01)	32.6 (± 0.02)	0.1 (± 0.00)
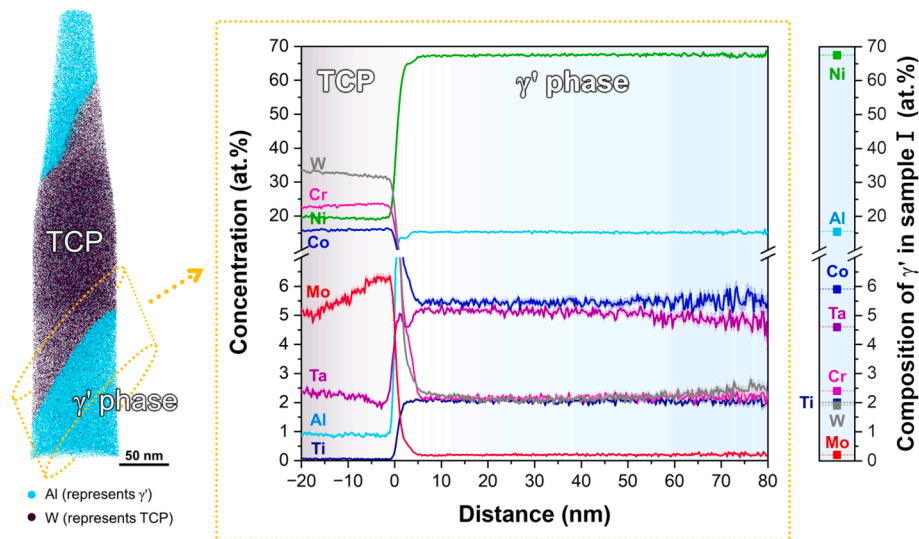
Fig. 4. A 3D atom map showing chemical distribution around the TCP/γ' structure after high-temperature exposure process and a proximity histogram at the TCP/γ' interface.

higher than that of the exposed sample. To exclude the influence of crystallographic orientation differences, the yield strength was converted to critical resolved shear stress (CRSS) by multiplying it by the highest $\{111\}\langle 1\bar{1}0\rangle_{\gamma/\gamma'}$ Schmid factors for each sample (0.44 for the unexposed and 0.41 for the exposed samples calculated from the EBSD orientation data). The cumulative distribution function (CDF) of the CRSS in Fig. 7 highlights the difference in strength between them. The mean CRSS were calculated to be 541 ± 27 and 489 ± 35 MPa for unexposed and exposed samples, respectively. The lower CRSS of the TCP-containing exposed sample indicates that despite the formation of TCP phases during the high-temperature exposure, the TCP phases resulted in a reduction in strength rather than causing a precipitation strengthening effect. Possible origins of strengthening mechanisms will be discussed in Section 4.2.

Secondly, the detailed observation of the influence of the TCP phase on the occurrence of slip in the surrounding region revealed the following results. Previous studies have shown that the TCP/γ' interface exhibits relatively weak bonding [23,39], which makes the TCP/γ' interface a potential crack initiation site due to decohesion of the interface. Additionally, a poor lattice coherency of TCP/γ' could accelerate the crack initiation and propagation at the interface [39]. However, in the present micropillar compression results, slip steps were observed a few tens of nanometers away from the TCP phase precipitate (see Fig. 5(b)), instead of the TCP/γ' interface decohesion reported in previous studies [23,39]. To be more quantitative, the distance between the slip steps and TCP phase was measured from 29 slip steps of 17 micropillars (Fig. 8). The distance from the interface to the slip trace

ranged from 0 to 300 nm, with a peak at 50 to 100 nm, while only a few slip steps were observed at the interface. This observation suggests that the TCP/γ' interface is not the weakest spot, instead, the neighboring region around 50–100 nm away from the TCP phase is comparatively easy to be sheared under deformation.

To understand the deformation behavior in greater detail, post-mortem TEM investigations were carried out on the TCP-containing micropillar presented in Fig. 5(b). The HAADF-STEM image, in Fig. 9(a) showcases the presence of a TCP phase (μ phase) in the upper and lower parts of the micropillar. The STEM-EDS map of Cr in Fig. 9(b), elucidates the microstructure of γ, γ', and TCP phase based on the distribution of Cr, since Cr tends to partition preferentially to the γ and TCP phases rather than the γ' precipitates [36,43]. The γ' phase surrounding the TCP phase was evident from the Cr map. Notably, in the magnified image in Fig. 9(c) and (d), the bright contrast lines, indicative of slip traces, can be observed running parallel to the TCP phase, with distinct slip traces occurring about 50 nm away from the TCP phase. These slip traces extended further, resulting in shearing of the γ' phases (indicated by the white arrow in Fig. 9(b)). Although there were fine slip traces even close to the TCP phases, majority was away from the TCP/γ' interface, especially the ones with strong contrast in Fig. 9(c) and (d). It is suggested that the local region of γ' precipitate near the TCP phase encountered increased resistance to deformation.

Additionally, to identify the types of these planar defects, the atomic stacking sequence of the $\{111\}_{\gamma'}$ near the TCP phase was investigated through atomic-resolution STEM imaging (Fig. 9(e)). The atomic configuration at the slip traces maintains a perfect FCC, *ABCABC*
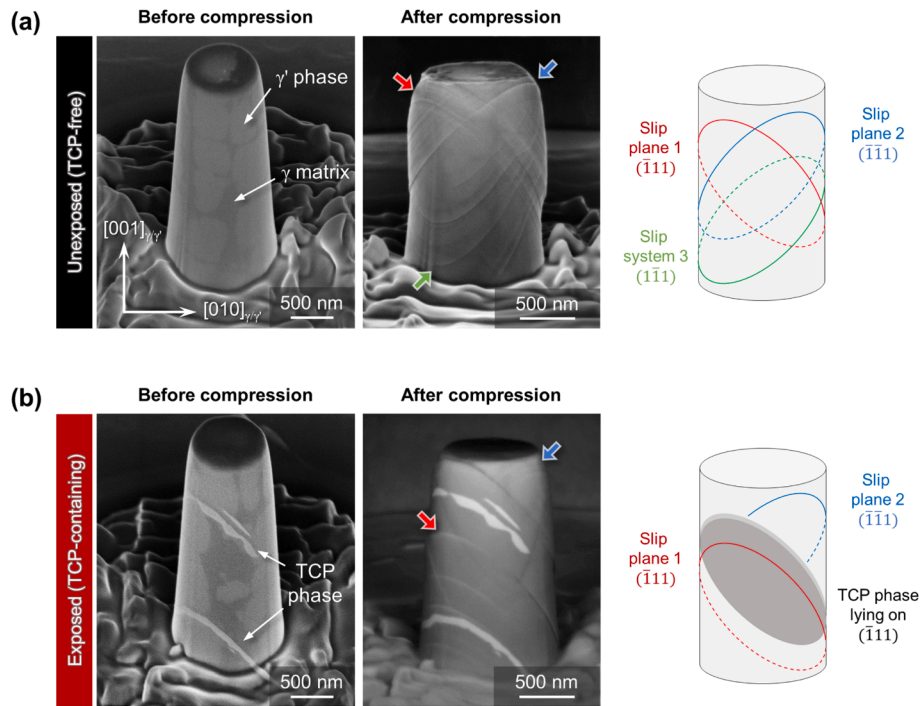
Fig. 5. Representative SEM images of micropillars and schematic diagrams depicting {111} octahedral slip traces, determined by directions and angles, after the compression test; **(a)** The unexposed (TCP-free) sample and **(b)** the exposed (TCP-containing) sample.
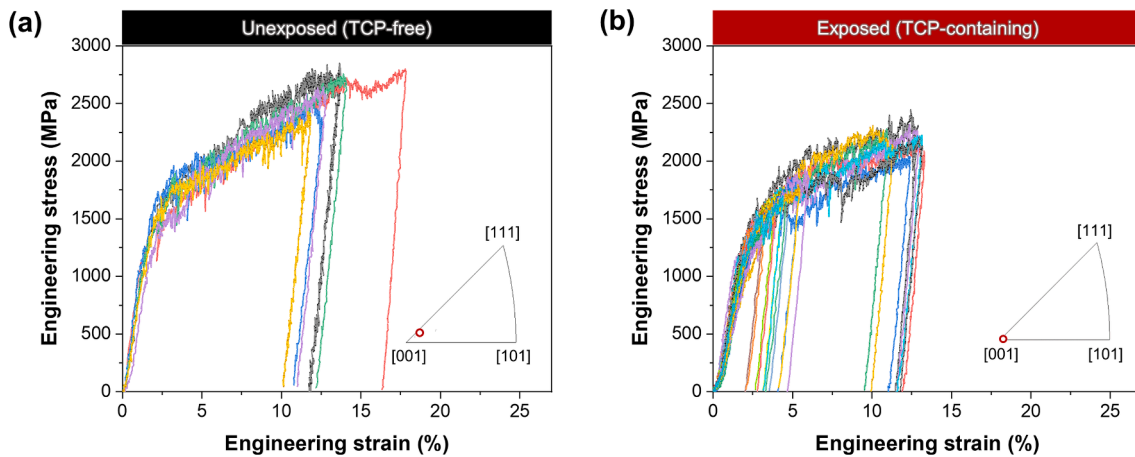
Fig. 6. The engineering strain–stress curves of **(a)** the unexposed (TCP-free) and **(b)** the exposed (TCP-containing) specimens.

sequence, indicating the occurrence of the antiphase boundary (APB) shearing mechanism instead of stacking faults, such as superlattice intrinsic stacking fault (SISF) and superlattice extrinsic stacking fault (SESF) [44–46].

4. Discussion

4.1. The slip behavior in the vicinity of the TCP phase

In the present study, fracture was observed neither inside the TCP phase nor at the interface, contrary to expectations of fracture occurring within the brittle TCP phase [23,39] or at the weak TCP/γ interface [23], where have been considered as crack initiation sites during tensile and impact testing. Remarkably, the slips were found to occur at a location approximately 50–100 nm away from the interface (refer to Figs. 8 and 9). To interpret the slip behavior near the interface, chemical composition and elastic strain aspects are discussed.

4.1.1. The effect of compositional gradient near the TCP/γ' interface

The formation of the TCP phase involves the consumption of refractory elements from the adjacent γ matrix, resulting in the dissolution of the γ matrix and the evolution of the γ' envelope surrounding TCP phases (refer to Section 3.2). During the process of γ'-forming elements diffusing from the TCP phase into the γ' phase, the rapid diffusion of Al and Ti at 1000°C resulted in a uniform concentration only after 30 min of heat treatment. However, Ta, due to its sluggish diffusion [40], accumulates near the interface (see Fig. 4). From the APT composition profile in Fig. 4, Ta concentration peaks 5 at.% at the TCP/γ' interface and gradually decreases to 4.5 at.% within the surrounding γ' phase. This non-uniform elemental distribution can affect the defect formation energies, such as APB energy, leading to inhomogeneous deformation behavior within the surrounding γ' phase. Hence, we intend to discuss the influence of the compositional distribution, influencing APB energy near the interface.

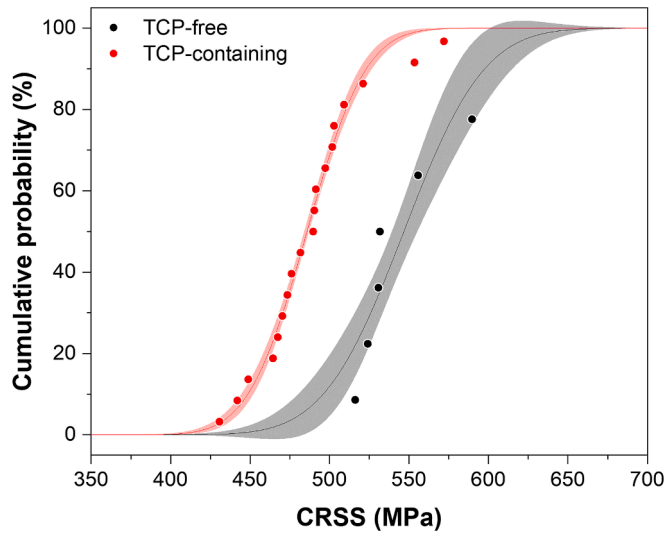Among the various strengthening mechanisms in superalloys, the γ'

Fig. 7. A CDF of CRSS measured from micropillar compression tests at room temperature. The grey and red-colored area indicate a 95% confidence level. (For interpretation of the references to colour in this figure legend, the reader is referred to the web version of this article.)
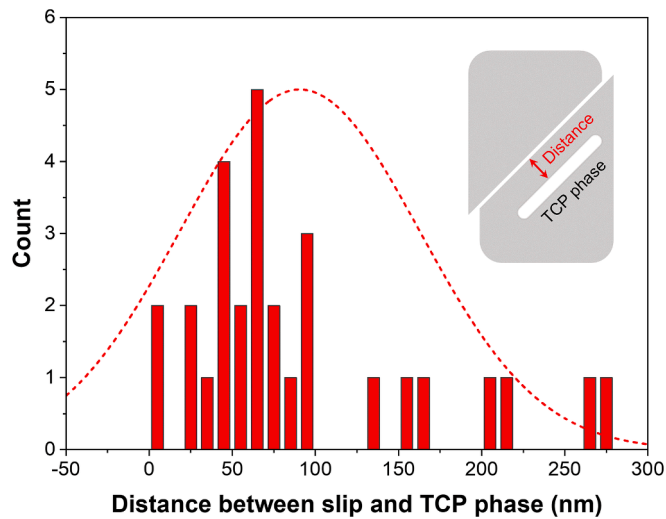

Fig. 8. A histogram of a distance between the slip trace and the TCP phase, measured from the deformed micropillar surface.

shearing mechanism is dominant at room temperature where diffusion-controlled dislocation climbing or Orowan strengthening is limited [47,48]. Particularly, W. Milligan and S. Antolovich [47] demonstrated that the γ' shearing mechanism is typically accompanied by the creation of APB at temperatures below 760°C, a phenomenon consistent with the observation in our result (see Fig. 9(e)). The formation of an APB between leading and trailing dislocations within ordered phases like γ' results in the creation of energetically unfavorable A–A and B–B bonds, thereby acting as obstacles to deformation (known as the order strengthening) [38]. Thereby, the stress required to cut the γ' phase is proportional to γ_{APB}/b, where γ_{APB} is APB energy and b is the magnitude of the Burgers vector [47–49].

From the obtained compositional profile near the TCP/γ' interface in Fig. 4, the APB energy of the γ' phase was estimated by employing the linear model described by Eq. (1) [50]:

$$\gamma_{APB} = \gamma_{APB}^o + \sum_{i=1}^{n} k_i c_i \tag{1}$$

where γ_{APB} is the APB energy, γ_{APB}^o is the APB energy for Ni₃Al (195 mJ/m²) [51], k_i is the coefficient for change in APB energy listed in Table 3, c_i is the concentration of element i in mole fraction, and n is the number of solute elements. The highest APB energy value was approximately 370 mJ/m² at the interface, and it gradually decreased below 360 mJ/m² as the distance from the interface increased (Fig. 10(a)). As a comparison, the APB energy of the γ' precipitate from the unexposed sample was also calculated which was 353 mJ/m² and plotted as a gray-colored dashed line in Fig. 10(a). This calculation suggests that the TCP-surrounding γ' has a higher APB energy compared to the intrinsic APB energy, i.e., other γ' precipitates away from TCP phases, and it progressively converges towards the intrinsic value as the distance from the interface increases. Moreover, it is observed that the position where the APB energy starts to decrease corresponds to the location where slip was frequently observed in the deformed micropillar (Fig. 8). Thus, this observation implies that a relatively high APB energy in the region within approximately 50 nm near the interface could induce a local order strengthening effect in that region.

To estimate the contributions of each element to the changes of APB energy, the differences in APB energies ($\Delta\gamma_{APB(i)}$) at a given distance x from the interface ($\gamma_{APB(i)}^x$) and at the interface ($\gamma_{APB(i)}^{int}$) were estimated by following equations and represented in Fig. 10(b).

$$\gamma_{APB(i)}^x = k_i c_i^x \text{ (at a distance } x) \tag{2}$$

$$\gamma_{APB(i)}^{int} = k_i c_i^{int} \text{ (at the interface)} \tag{3}$$

$$\Delta\gamma_{APB(i)} = \gamma_{APB(i)}^x - \gamma_{APB(i)}^{int} \tag{4}$$

where c_i^x and c_i^{int} denote the concentration of element i at a distance x and the interface, respectively. As a result, Cr, Mo, and Ti exhibit nearly constant contributions to the total APB energy independent on the distance from the interface. However, W and Ta, with low interdiffusion coefficients in γ' precipitates [40], exhibit fluctuations as the distance varies. Notably, the contribution of Ta is decreased about 13 mJ/m² at a distance of 80 nm from the interface due to its high coefficient (k_{APB}) for APB energy (i.e., 27.1 mJ/m²), and it is expected to keep decreasing beyond 80 nm. Thus, it is apparent that the compositional profile of Ta dominantly influences the variation of APB energy in the local region near the TCP phase.

Consequently, the compositional gradient near the TCP/γ' interface due to the sluggish diffusion behavior of Ta could be a one of the factors contributing to the observed slip suppression near the interface (Fig. 8) by inducing a local order strengthening effect.

4.1.2. The effect of elastic strain at the TCP/γ' interface

Based on the crystallographic relationship and measured lattice parameters of the TCP and γ' phases, the misfit strain at the TCP/γ' interface can be estimated. The atomic structure model of the μ phase (Co₇Mo₆) is illustrated in Fig. 11(a), composed of alternately stacked Kagomé, CN14, CN15, and triple layer of Laves phase building blocks [35,52]. Additionally, Fig. 11(b–d) displays the (001)ᵤ atomic layers of Kagomé, CN14, and CN15, respectively, which are possible interface layers. However, the TEM results did not conclusively clarify which of these layers matched with the (11$\bar{1}$)ᵧ' layer (Fig. 11(e)). Nevertheless, considering the flat TCP/γ' interface, it is presumed that the layer with the highest coherency would match with the (11$\bar{1}$)ᵧ' planes. Based on this assumption, the C15 layer (Fig. 11(d)), which has the most similar symmetry and atomic distance to the (11$\bar{1}$)ᵧ' layer among the listed (001)ᵤ layers, was selected for the misfit strain estimation (Fig. 11(f)). The misfit strain in the case of Fig. 11(f) was estimated using the following equation.
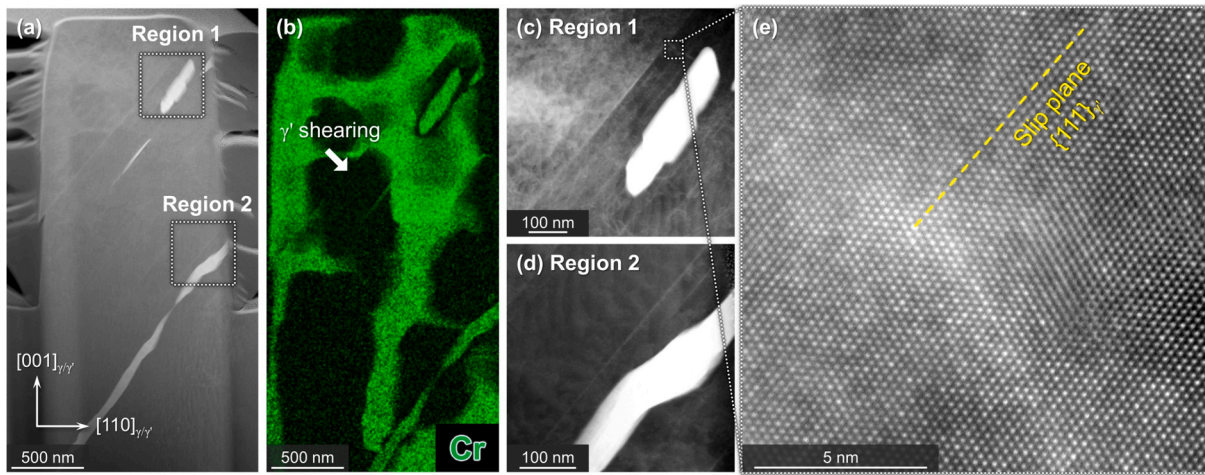
Fig. 9. The cross section of a 11% deformed micropillar in Fig. 5(b) representing slip behavior near TCP phase. **(a)** A HAADF STEM image, **(b)** a distribution map of Cr in STEM EDS showing γ/γ'/TCP structure, **(c, d)** magnified view of regions of interest in the image **(a)**, and **(e)** an atomic-resolution HAADF STEM image showing a perfect atomic stacking sequence of $\{111\}_{\gamma'}$ which indicates antiphase boundary (APB) mechanism.

Table 3

Coefficients ($k_{i,APB}$) for antiphase boundary (APB) energy calculation in Eq. (1) [50].

Element	Cr	Mo	W	Ta	Ti
mJ/m^2	–1.7	–1.7	4.6	27.1	15.0

$$\frac{2 \times (d_{C15} - d_{\gamma'})}{(d_{C15} + d_{\gamma'})} \times 100\% \tag{5}$$

where, d_{C15} and $d_{\gamma'}$ are the atomic distance on the C15 layer and $(11\bar{1})_{\gamma'}$ layer, which were measured from the HR-TEM image at room temperature (Fig. 2), respectively. In the result, the misfit strain was measured as 7.5%, suggesting that the TCP/γ' interface has semicoherent relationship [38], thus the misfit could cause elastic strain field on the γ' phase near the interface. Eventually, it may offer an additional deformation resistance in the vicinity of the TCP phase.

Another possibility is the elastic mismatch between two different phases which can hinder dislocation motion near the phase boundary [53]. The μ phase has been reported to have a higher elastic modulus (238 GPa) than the γ' phase (202 GPa) [13], thus inducing an elastic strain field near the TCP/γ' interface. Also, the formation of large-scale residual stress fields in the vicinity of the TCP phase caused by a mismatch of the coefficients of thermal expansion of the TCP and γ' phases, can alter the local driving force for dislocation motion.

### 4.2. Degradation of yield strength during high-temperature exposure

Although the TCP phase appears to induce a local order strengthening effect in the surrounding γ' phase by influencing the APB energy and elastic strain field, making them a contributing factor to the strengthening effect at the interface, these effects are not dominant in yield strength. As represented in the stress–strain curves in Fig. 6(a) and (b), the strength of the TCP-containing exposed samples was lower than that of the TCP-free unexposed samples even though the TCP phase interrupted the slip behavior (refer to Fig. 5(b)). Further, the reason why the strengthening effect is negligible in the presence of the TCP phase could be its low volume fraction and plate-like morphology. The probability of interaction between the TCP phase and slip occurring parallel to the $\{111\}_{\gamma/\gamma'}$ planes (where the TCP phase is located) is considered to be low. Therefore, while the TCP phase does hinder slip activity, the overall decrease in yield strength is primarily due to the softening effects caused by the microstructural changes that occurred during the exposure process. In the following sections the effect of the γ' phase volume
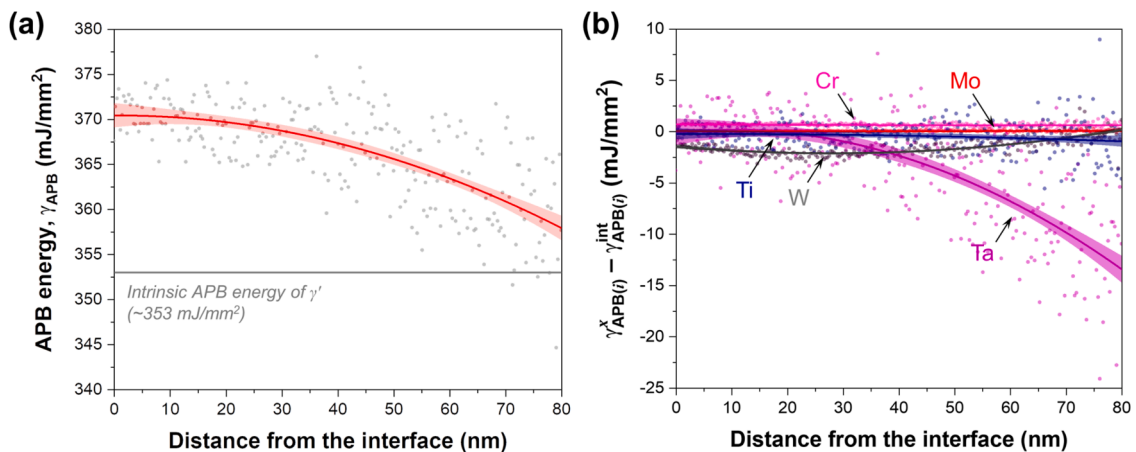
Fig. 10. (a) A variation of antiphase boundary (APB) energy (γ_{APB}) in the γ' as a function of the distance from the interface and **(b)** contributions of each element in the γ_{APB}, where $\gamma_{APB(i)}^{x}$ and $\gamma_{APB(i)}^{int}$ denote the γ_{APB} at a distance x and the interface for the element i, respectively. The colored bands indicate 95% confidence level of each data.
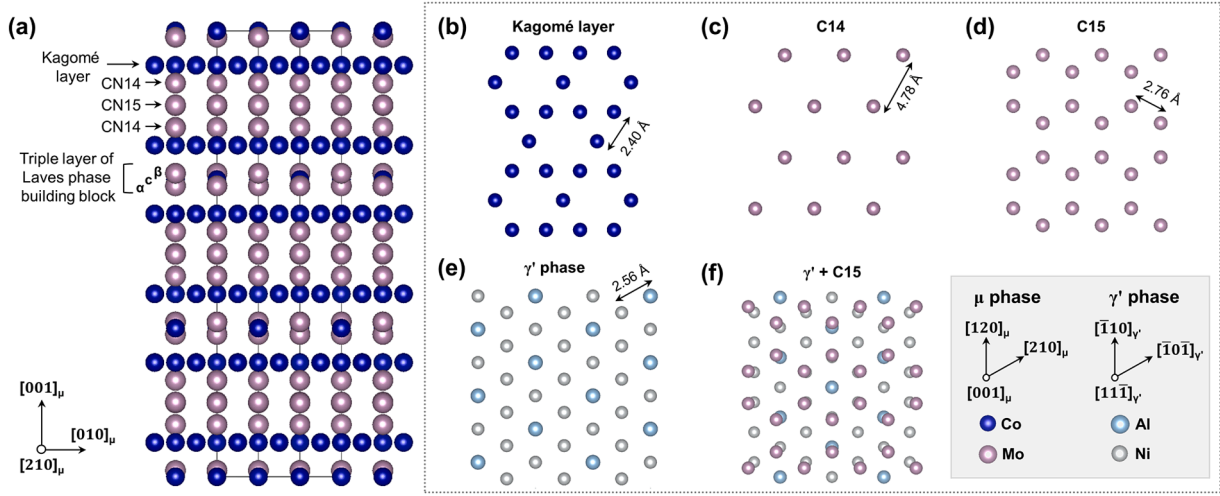
Fig. 11. (a) The atomic structure model of the μ phase (Co$_7$Mo$_6$), $(001)_\mu$ atomic configurations of (b) Kagomé layer (c) CN14 layer, and (d) CN15 layer. (e) The $(11\bar{1})_\gamma$ atomic layer, and (f) overlapped atomic configuration of (d) and (e) showing semicoherent interface of the TCP/γ'.
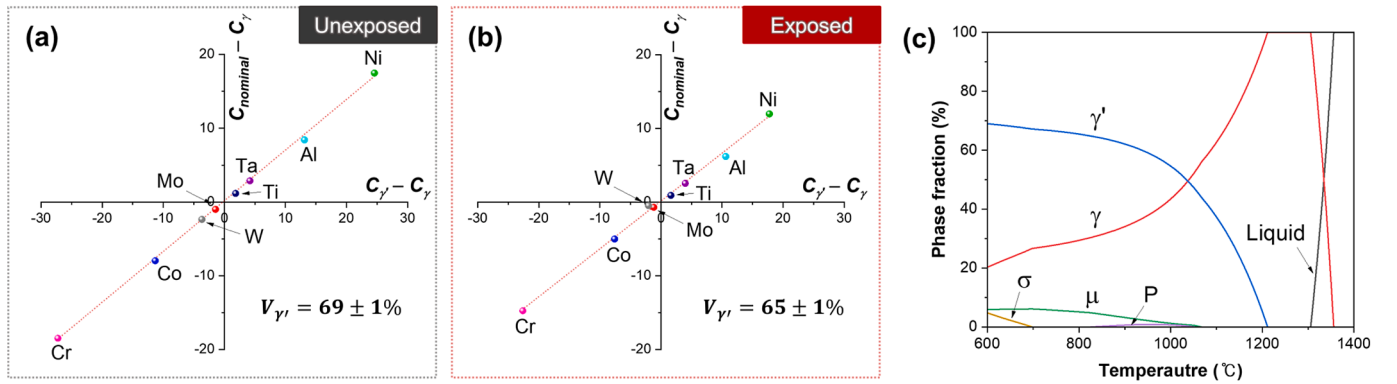
Fig. 12. Lever rule plots for the γ' volume fraction ($V_{\gamma'}$) calculation in the (a) unexposed and (b) exposed specimens, and (c) a temperature dependence of volume fraction of each phase in the equilibrium state calculated by JMatPro software with TTNi8 database.

fraction and solid solution strengthening in the γ matrix are discussed.

4.2.1. Reduction in the γ' phase volume fraction

The influence on volume fraction of γ' phase during high temperature exposure significantly affects the strength of γ/γ' dual-phase superalloys. As previously noted, an additional stress is required to cut the ordered γ' phase, resulting in higher CRSS with higher volume fraction of γ' phase [54]. The variation in the volume fraction of the γ' precipitate during the exposure can be estimated from the variations in the chemical compositions of γ and γ' phases and calculated using lever rule. As the volume fraction of the TCP phases is approximately estimated as 1.1% in the exposed specimen (Fig. S3), it can be assumed that the microstructure consists of γ and γ' phases. Then, the volume fraction of the γ' precipitate can be calculated using the lever rule based on the mass balance equation [55,56]:

$$V_{\gamma'} = \frac{C_{nom} - C_\gamma}{C_{\gamma'} - C_\gamma} \qquad (6)$$

Table 4
Coefficients ($k_{i,ss}$) for solid solution strengthening of γ matrix calculation in Eq. (7) [58].

Element	Al	Co	Cr	Mo	Ta	W	Ti
MPa/at.%	225	29.4	337	1015	1191	977	775

where $V_{\gamma'}$ is the volume fraction of the γ' precipitate, C_{nom} is the nominal concentration, C_γ is the concentration in γ matrix, and $C_{\gamma'}$ is the concentration in γ' precipitate. The lever rule plots of the alloying elements for γ' volume fraction calculation are illustrated in Fig. 12. The γ' volume fractions were obtained from the slope of the fitted lines. The measured volume fraction is 69 ± 1% for the unexposed sample (Fig. 11 (a)), and it is reduced to 65 ± 1% for the exposed sample (Fig. 11(b)). The reduction in the volume fraction of γ' phase is attributed to the low equilibrium volume fraction of γ' phase at 1000°C (i.e., 54.6%), as indicated by thermodynamic calculation result in Fig. 11(c). Thus, the reduction in the γ' volume fraction, which is of the strengthening factors, is considered to contribute to the softening behavior during high-temperature exposure.

4.2.2. Reduction in solid solution strengthening effect in the γ matrix

Solid solution strengthening of the γ matrix is also a major strengthening mechanism in the Ni-based superalloys. In the deformation process in the γ matrix, dislocations are disrupted by the interaction with solute atoms [54]. The APT analysis revealed a decrease in the concentration of refractory elements within the γ matrix due to the formation of the TCP phase, with Co decreasing by −3.0%, Cr by −3.7%, and W by −1.9%. Such changes in concentration can contribute to variations in solid solution strengthening effect within the γ matrix. From the compositional data in Table 2, the contribution of the individual element present in solid solution contributing to the strengthening of the γ matrix can be evaluated using the following relation [57].
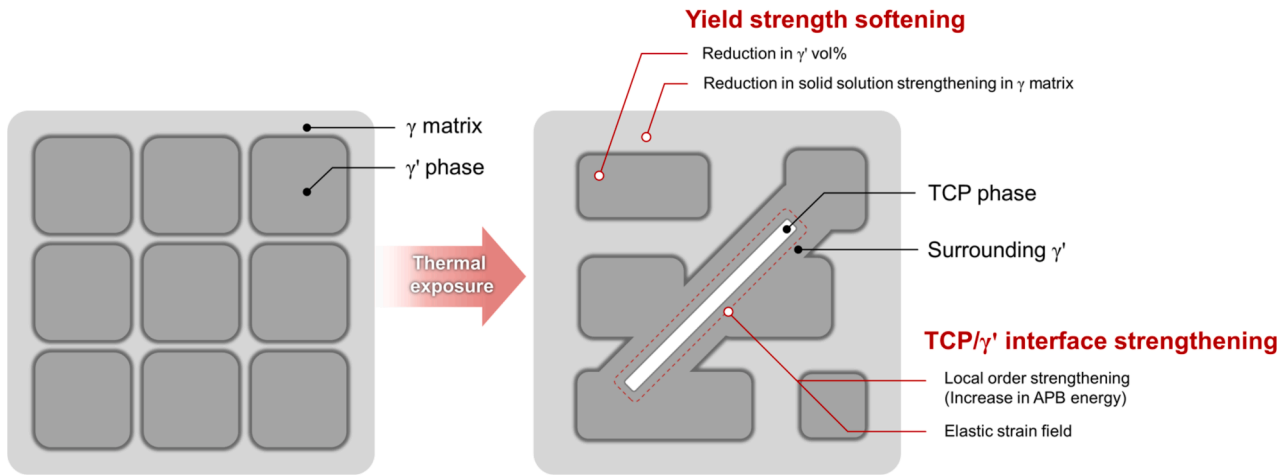
Fig. 13. A schematic showing the deformation behavior and mechanical properties in the vicinity of the TCP phase.

$$\Delta\sigma_{ss} = \left(\Sigma_i k_i^{\frac{1}{n}} c_i \right)^n \qquad (7)$$

where k_i is the coefficient for solid solution strengthening listed in Table 4, c_i is atomic fraction, and n is strengthening exponent with a value of 0.5. From the above relation, the solid solution strengthening is estimated to be 335 ± 0.4 MPa for the unexposed specimen and 312 ± 9.6 MPa for the exposed specimen. It indicates that the variation of concentration in the γ matrix during high-temperature exposure results in a reduction of the solid solution strengthening effect around 23 MPa. Therefore, despite the strengthening effect could be introduced by the TCP phase itself, the softening occurs due to the reductions in the volume fraction of γ' phase and the solid solution strengthening in the γ matrix resulting in overall degradation of strength after high temperature exposure.

A schematic in Fig. 13 illustrates the observed deformation behavior and mechanical properties in the vicinity of the TCP phase. After high-temperature exposure, the TCP phases are formed and surrounded by the γ' phases. During this microstructural evolution, the TCP phases supply the γ'-forming elements to the surrounding γ' phase, creating a locally Ta-rich regions nearby the TCP/γ' interface. The excess of Ta increases the APB energy, thereby inducing a local order strengthening effect. Additionally, the TCP/γ' interface have a misfit of 7.5%, resulting in the formation of an elastic strain field. This local order strengthening and elastic strain field enhance the slip resistance in the vicinity of the interface. Meanwhile, yield strength softening occurred in the region containing γ, γ', and TCP phases due to the reduction in the γ' volume fraction and the diminished solid solution strengthening effect in the γ matrix caused by the depletion of refractory elements through the formation of the TCP phases.

5. Conclusion

The influence of the TCP phase formation on the deformation behavior and mechanical properties in a single crystal Ni-based super-alloy were systematically investigated through micro-scale mechanical investigations and atomic-scale compositional analysis. The conclusions are summarized as follows:

1. The TCP phase affects the slip behavior by hindering the activation of the non-parallel slip systems. As a result, in the TCP-free unexposed sample, multiple slip systems were observed, whereas in the TCP-containing exposed sample, only a single slip system was activated.
2. The formation of the TCP phase changes local chemical distribution in the surrounding γ' precipitate, increasing the APB energy near the TCP phase. In addition, the TCP phase induces an elastic strain field

in the surrounding γ' precipitate due to the lattice misfit. These effects prevent the TCP/γ' interface from being the weakest spot, causing the slip to occur in the regions more than 50–100 nm away from the interface.
3. Although the TCP phase does affect the deformation behavior, in terms of the overall strength, other mechanisms from the surrounding γ/γ' primarily determines the yield strength. During the high-temperature exposure, reductions in volume fraction of the γ' precipitate and the solid solution strengthening effect in the γ matrix contribute the decrease in the yield strength.

CRediT authorship contribution statement

Declaration of competing interest

The authors declare that they have no known competing financial interests or personal relationships that could have appeared to influence the work reported in this paper.

Acknowledgment

www.kit.edu).

Appendix A. Supplementary data

Supplementary data to this article can be found online at https://doi.org/10.1016/j.matdes.2025.113600.

Data availability

Data will be made available on request.

References

[1] R.C. Reed, The Superalloys: Fundamentals and Applications, Book (2006).
[2] M. Ishikawa, T. Komori, M. Terauchi, J. Yasuraoka, Tech. Rev. Mitsubishi Heavy Ind. 45 (2008) 15–17.
[3] T. Saito, H. Harada, T. Yokokawa, M. Osawa, K. Kawagishi, S. Suzuki, Mater. Trans. 65 (2024) 1443–1457.
[4] G. Gudivada, A.K. Pandey, J. Alloys Compd. 963 (2023) 171128.
[5] J. Zhang, F. Lu, T. Huang, R. Li, G. Zhang, L. Liu, Mater. Sci. Eng. A 881 (2023) 145382.
[6] R.C. Reed, T. Tao, N. Warnken, Acta Mater. 57 (2009) 5898–5913.
[7] R.A. MacKay, T.P. Gabb, J.L. Smialek, M.V. Nathal, N.A.S.A. Tech, Rep. (2009) 1–39.
[8] S. Wöllmer, T. Mack, U. Glatzel, Mater. Sci. Eng. A 319–321 (2001) 792–795.
[9] M. Velasco-Castro, F.D. León-Cázares, E.I. Galindo-Nava, Mater. Des. 247 (2024) 113416.
[10] C. Liu, W. Yang, J. Qin, P. Qu, H. Fu, Q. Wang, J. Zhang, L. Liu, J. Mater. Sci. Technol. 202 (2024) 165–173.
[11] X. Su, Q. Xu, R. Wang, Z. Xu, S. Liu, B. Liu, Mater. Des. 141 (2018) 296–322.
[12] V.C.I. Strutt, B.M. Jenkins, J.M. Woolrich, M. Appleton, M.P. Moody, P.A.J. Bagot, J. Alloys Compd. 949 (2023) 169861.
[13] H. ur Rehman, K. Durst, S. Neumeier, A.B. Parsa, A. Kostka, G. Eggeler, M. Göken, Mater. Sci. Eng. A 634 (2015) 202–208.
[14] K. Matuszewski, A. Müller, N. Ritter, R. Rettig, K.J. Kurzydłowski, R.F. Singer, Adv. Eng. Mater. 17 (2015) 1127–1133.
[15] Y. Cheng, X. Zhao, W. Xia, Q. Yue, Y. Gu, Z. Zhang, Mater. Des. 237 (2024) 112582.
[16] Y. Zhao, X. Zhao, X. Qi, Y. Cheng, J. Zou, Y. Wang, X. Qu, Q. Yu, Z. Zhang, Acta Mater. 275 (2024) 120056.
[17] C.M.F. Rae, R.C. Reed, Acta Mater. 49 (2001) 4113–4125.
[18] W. Xia, X. Zhao, L. Yue, Z. Zhang, J. Alloys Compd. 819 (2020) 152954.
[19] J. Li, J. Sun, J. Liu, X. Sun, J. Mater. Sci. Technol. 173 (2024) 149–169.
[20] Y. Cheng, X. Zhao, L. Qiao, Q. Yue, J. Wang, Q. Pan, W. Xia, Y. Gu, Z. Zhang, Mater. Sci. Eng. A 915 (2024) 147232.
[21] M. Pessah-Simonetti, P. Caron, T. Khan, J. Phys. IV 3 (1993) 347–350.
[22] A. Volek, R.F. Singer, R. Buergel, J. Grossmann, Y. Wang, Metall. Mater. Trans. A Phys. Metall. Mater. Sci. 37 (2006) 405–410.
[23] Q. Shi, X. Ding, J. Chen, X. Zhang, Y. Zheng, Q. Feng, Metall. Mater. Trans. A 45 (2014) 1665–1669.
[24] W. Guo, H. Zhao, Y. Ru, Y. Pei, J. Wang, Q. Liu, X. Li, H. Wang, S. Zhang, S. Gong, S. Li, Crystals 12 (2022) 1446.
[25] A.C. Yeh, S. Tin, Metall. Mater. Trans. A Phys. Metall. Mater. Sci. 37 (2006) 2621–2631.
[26] P. Zhao, G. Xie, C. Chen, X. Wang, P. Zeng, F. Wang, J. Zhang, K. Du, Acta Mater. 236 (2022) 118109.
[27] Z. Wang, Y. Li, H. Zhao, L. Chen, Z. Zhang, D. Shen, M. Wang, J. Alloys Compd. 782 (2019) 1–5.
[28] Q. Chen, N. Jones, D. Knowles, Acta Mater. 50 (2002) 1095–1112.
[29] K. Cheng, C. Jo, T. Jin, Z. Hu, J. Alloys Compd. 509 (2011) 7078–7086.
[30] J.X. Yang, Q. Zheng, X.F. Sun, H.R. Guan, Z.Q. Hu, Scr. Mater. 55 (2006) 331–334.
[31] L. Haußmann, S. Neumeier, M. Kolb, J. Ast, G. Mohanty, J. Michler, M. Göken, Miner. Met. Mater. Ser. (2020) 273–281.
[32] Y. Kalchev, R. Zehl, T. Piotrowiak, A. Kostka, D. Naujoks, J. Pfetzing-Micklich, A. Ludwig, Metall. Mater. Trans. A Phys. Metall. Mater. Sci. 54 (2023) 1526–1534.
[33] A. Bhowmik, J. Lee, S. Adande, M. Wang-Koh, T.S. Jun, G. Sernicola, T. Ben Britton, C.M.F. Rae, D. Balint, F. Giuliani, Materialia 9 (2020) 100635.
[34] K. Arora, K. Kishida, K. Tanaka, H. Inui, Acta Mater. 138 (2017) 119–130.
[35] W. Luo, Z. Xie, P.-L. Sun, J.-S.-K.-L. Gibson, S. Korte-Kerzel, Acta Mater. 246 (2023) 118720.
[36] S. Lee, J. Do, K. Jang, H. Jun, Y. Park, P. Choi, Scr. Mater. 222 (2023) 115041.
[37] S. Schröders, S. Sandlöbes, B. Berkels, S. Korte-Kerzel, Acta Mater. 167 (2019) 257–266.
[38] D.A. Porter, K.E. Easterling, K.E. Easterling, Phase Transformations in Metals and Alloys, CRC Press, 2009.
[39] M. Simonetti, P. Caron, Mater. Sci. Eng. A 254 (1998) 1–12.
[40] J. Chen, L. Zhang, X.G. Lu, Intermetallics 102 (2018) 11–20.
[41] J. Zhang, T. Huang, F. Lu, K. Cao, D. Wang, J. Zhang, J. Zhang, H. Su, L. Liu, Scr. Mater. 204 (2021) 114131.
[42] A. Mottura, N. Warnken, M.K. Miller, M.W. Finnis, R.C. Reed, Acta Mater. 58 (2010) 931–942.
[43] Z. Peng, I. Povstugar, K. Matuszewski, R. Rettig, R. Singer, A. Kostka, P.P. Choi, D. Raabe, Scr. Mater. 101 (2015) 44–47.
[44] X. Wu, S.K. Makineni, C.H. Liebscher, G. Dehm, J. Rezaei Mianroodi, P. Shanthraj, B. Svendsen, D. Bürger, G. Eggeler, D. Raabe, B. Gault, Nat. Commun. 11 (2020) 1–13.
[45] T.M. Smith, B.D. Esser, N. Antolin, G.B. Viswanathan, T. Hanlon, A. Wessman, D. Mourer, W. Windl, D.W. McComb, M.J. Mills, Acta Mater. 100 (2015) 19–31.
[46] T.M. Smith, B.D. Esser, B. Good, M.S. Hooshmand, G.B. Viswanathan, C.M.F. Rae, M. Ghazisaeidi, D.W. McComb, M.J. Mills, Metall. Mater. Trans. A Phys. Metall. Mater. Sci. 49 (2018) 4186–4198.
[47] W.W. Milligan, S.D. Antolovich, Metall. Trans. A 18 (1987) 85–95.
[48] P. Zhang, Y. Yuan, S.C. Shen, B. Li, R.H. Zhu, G.X. Yang, X.L. Song, J. Alloys Compd. 694 (2017) 502–509.
[49] R.C. Reed, C.M.F. Rae, Physical Metallurgy of the Nickel-Based Superalloys, Elsevier, Fifth Edit, 2014.
[50] D.J. Crudden, A. Mottura, N. Warnken, B. Raeisinia, R.C. Reed, Acta Mater. 75 (2014) 356–370.
[51] T. Kruml, E. Conforto, B. Lo Piccolo, D. Caillard, J.L. Martin, Acta Mater. 50 (2002) 5091–5101.
[52] K.S. Kumar, P.M. Hazzledine, Intermetallics 12 (2004) 763–770.
[53] K. Jagannadham, M.J. Marcinkowski, J. Mater. Sci. 15 (1980) 309–326.
[54] A. Vattré, B. Devincre, A. Roos, Intermetallics 17 (2009) 988–994.
[55] D. Blavette, A. Bostel, J.M. Sarrau, B. Deconihout, A. Menand, Nat. 1993 3636428 363 (1993) 432–435.
[56] I. Povstugar, P.P. Choi, S. Neumeier, A. Bauer, C.H. Zenk, M. Göken, D. Raabe, Acta Mater. 78 (2014) 78–85.
[57] D. Canadinc, H. Sehitoglu, H.J. Maier, Y.I. Chumlyakov, Acta Mater. 53 (2005) 1831–1842.
[58] F. Diologent, P. Caron, Mater. Sci. Eng. A 385 (2004) 245–257.